Lithium Stripping: Anisotropic Evolution and Faceting of Pits Revealed by Operando 3-D Microscopy

Journal:	*Journal of Materials Chemistry A*
Manuscript ID	TA-ART-04-2021-003333.R1
Article Type:	Paper
Date Submitted by the Author:	16-Jun-2021
Complete List of Authors:	Sanchez, Adrian; University of Michigan, Mechanical Engineering Kazyak, Eric; University of Michigan, Mechanical Engineering Chen, Yuxin; University of Michigan, Mechanical Engineering Lasso, Jose; University of Michigan, Mechanical Engineering Dasgupta, Neil; University of Michigan, Mechanical Engineering; Materials Science & Engineering

SCHOLARONE™
Manuscripts

1 **Lithium Stripping: Anisotropic Evolution and Faceting of Pits Revealed by *Operando* 3-D Microscopy**

2

3   Adrian J. Sanchez[1], Eric Kazyak[1], Yuxin Chen[1], Jose Lasso[1], Neil P. Dasgupta[1,2*]

4   [1] Department of Mechanical Engineering, University of Michigan, Ann Arbor, MI 48109, USA

5   [2] Department of Materials Science & Engineering, University of Michigan, Ann Arbor, MI 48109, USA

6   *Corresponding Author: ndasgupt@umich.edu

7

8 **Abstract**

9   A critical challenge that hinders the development of next-generation Lithium (Li) metal batteries is the poor reversibility

10 of Li plating and stripping. This study explores the dynamic evolution of Li metal surface morphology during stripping. A

11 platform for *operando* focus variation microscopy is presented and used to reveal strong anisotropy and faceting in

12 surface pits, which correlates with surface microstructure. Specifically, this study: 1) maps out the dynamic morphological

13 evolution of individual pits in 3-dimensions; 2) demonstrates anisotropic pit expansion in both in-plane and through-plane

14 directions; 3) correlates anisotropy with surface grain boundaries and crystallographic texture; and 4) demonstrates

15 faceted edges in pits, which align within individual grain orientations. The results presented provide greater insight into

16 the fundamental nature of Li stripping reactions and raise new questions about the role of microstructure in reversible

17 cycling of Li metal.

18 **<u>Introduction</u>**

19   A promising pathway to improve the energy density of next-generation batteries beyond Li-ion technology is to

20 incorporate a Lithium (Li) metal anode. Li metal anodes have a high specific capacity (3860 mAh/g), low electrochemical

21 potential (-3.04 V vs SHE), and can enable high-energy-density battery chemistries, including Li-Air and Li-S.[1] However,

22 factors such as poor Coulombic efficiency (CE) and instability against common liquid electrolytes have prevented the

23 widespread use Li metal anodes in rechargeable batteries.

24   The interplay between the instability of Li metal against common liquid electrolytes and its dynamic

25 morphological evolution hinders cycling performance.[2] When Li is exposed to a liquid electrolyte, a spontaneous solid

26 electrolyte interphase (SEI) forms. Additionally, 3-dimensional surface morphologies form during cycling, such as

27 dendrites and pits. These structures increase the area of the electrode-electrolyte interface and promote further SEI

28   formation. Furthermore, significant capacity loses occur when active Li is isolated from the electrode and "dead" Li

29   forms.[3–5]

30   Various strategies have been developed to address the known problems of Li metal anodes. One common

31   approach has been to modify the structure of the electrode. This includes the design of the three-dimensional host

32   architectures [6,7] and mechanical deformation of the electrode surface.[8,9] Other methods include chemical or structural

33   modifications of the electrode-electrolyte interface,[10–12] and variations in the electrolyte composition.[13,14] Improved

34   performance has been achieved through the application of these strategies, but the CE of state-of-the-art Li metal anodes

35   has plateaued to ~99.5% in recent years.[15] Therefore, strategies to address the remaining ~0.5% are critical to extend the

36   cycle life of Li-metal batteries. Fundamental studies have identified factors that contribute to low CE, including current

37   density and depth of discharge, low stack pressure, electrolyte composition, and dead Li formation.[3,16–18] However, further

38   exploration into the mechanisms that dictate irreversibility are needed to improve the Coulombic efficiency of Li metal

39   anodes.

40   *Operando* analyses have provided detailed insight into the dynamic evolution of the Li surface during cycling.[19–22]

41   These studies have provided a deeper understanding of how Li metal nucleates,[23–26] grows [27] and transitions to dead Li.[3–5]

42   However, an aspect of cycling that has not been explored extensively is the dynamic evolution of pits during the stripping

43   half-cycle. Recent studies have shown that pit formation plays a non-negligible role in Li metal anode performance.[28–30]

44   We have previously applied *operando* video microscopy to show that dendrites can preferentially nucleate along the

45   perimeter of pits formed in the previous half-cycle, and that this nucleation within pits leads to improved reversibility

46   when compared to nucleation at singular points along the electrode surface.[30] Furthermore, the reversibility of individual

47   dendrites was observed to be sensitive to the size of the pits within which nucleation occurred. However, the complete

48   mechanisms that link pit formation to dendrite nucleation and reversibility are not fully understood. Therefore, an

49   improved understanding of how pit geometry dynamically evolves, and the influence of electrode surface properties on pit

50   morphology, are critical for optimizing the CE and cycle life of Li metal batteries.

51   Previous studies have demonstrated improved performance by controlling the heterogeneity of the initial Li metal

52   surface through mechanical deformation,[8,9] surface coatings,[10,11,31] 3-dimensional architectures, [6,7] and *in situ*

53   electrochemical treatments.[32,33] These studies illustrate the critical importance of the initial Li metal surface on long-term

54   cycling. This is because the initial surface determines the electrode morphology and reversibility during the first cycle,

55   which directly impacts the extended cycle life. It has also been previously demonstrated that the initial surface

56   microstructure, including grain boundaries, impacts the nucleation of both dendrites and pits.[30] However, an improved

57   fundamental understanding of pit nucleation and growth, and how this relates to surface microstructure, is needed to

58   reveal the relationships between initial surface heterogeneity and long-term cyclability of Li metal anodes.

59   In this study, we explore the dynamic morphological evolution of pits during stripping. A platform for plan-view

60   *operando* video microscopy was previously introduced to study the relationships between nucleation, morphology, and

61   reversibility on a Li metal anode.[30] Herein, we expand upon this platform to capture 3-dimensional topographical maps of

62   the Li surface with focus variation microscopy.[34] This enables quantitative measurements of the nucleation and growth of

63   pits along the Li surface. Using the 3-D microscopy platform, this study: 1) delineates the morphological evolution of

64   individual pits in 3-dimensions; 2) demonstrates anisotropic growth of pits along in-plane and through-plane directions; 3)

65   correlates anisotropic pit expansion with surface grain boundaries and crystallographic texture; 4) demonstrates faceted

66   edges in pits, which are influenced by individual grain orientations.

67   **Results and Discussion**

68   **Focus Variation Microscopy for 3-D Dimensional Analysis**

69   The plan-view *operando* video microscopy platform implemented in our previous study was updated to achieve high-

70   magnification imaging.[30] This cell design is based on a concentric ring counter electrode, which is positioned with a

71   vertical offset from the Li metal working electrode. This geometry allows optical access to a wide field of view (a 5mm

72   electrode) while maintaining a uniform current density (<2% variation) along the entire working electrode surface. Further

73   details of the cell geometry used in this study, including COMSOL modeling of the current distribution profile, are

74   provided in the Supplementary Information.

75   The upgraded visualization cell was integrated with a Keyence VHX-7000 optical microscope. This digital

76   microscope can perform focus variation microscopy, which captures the areal surface topography of a sample.[34] Figure 1

77   shows the application of this new capability on a stripped Li electrode. First, the motorized objective scans along the out-

78   of-plane-axis and captures images of the Li surface at various focal planes. An encoder integrated into the objective

79   stepper motor records the position of each image along the out-of-plane axis with a spatial resolution of 100 nm. These

80   images are collected into a vertical stack where the objective position is used to determine the depth of each plane. A

81   depth-from-defocus (DOD) algorithm is then applied to identify which plane produces the highest focus quality for a

82   given pixel.[35] Focus quality is quantified by calculating the standard deviation of surrounding pixel grey values, where a

83 higher standard deviation indicates stronger contrast between pixels and better focus quality. Once all pixels have been

84 assigned to corresponding planes, a composite optical image is produced with the entire field-of-view in focus (Figure

85 1B). Furthermore, the depth of each pixel is quantified based on the position of the corresponding plane. This depth

86 information enables 3-dimensional reconstructions of the electrode surface, as shown in Figures 1 C-E. The 3-dimensional

87 information allows for quantitative analysis of the surface topography. This microscopy technique has been previously

88 used for applications ranging from archaeology to metrology for additive manufacturing.[36,37]
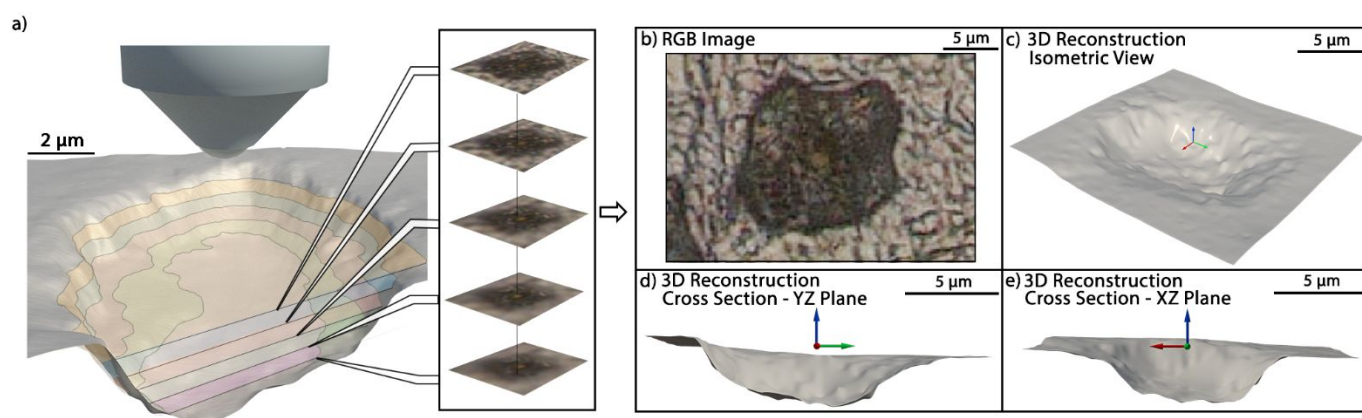
89

Figure 1. a) Schematic depiction of focus variation microscopy, where a focal series is captured and saved as a vertical image stack. After post-processing, b) the output is a composite optical image of the pit, which enables 3D reconstruction of the pit from c) an isometric view, and cross sections of the pit along the d) YZ and e) XZ-planes.

90 To validate the applicability of this 3-dimensional imaging capability for Li metal anodes, focus variation

91 microscopy and atomic force microscopy (AFM) were performed on the same electrodes. Three different samples (labeled

92 Pit A, Pit B, and Pit C in Figure 2) were extracted from Li-Li symmetric coin cells, where varying amounts of charge were

93 stripped in each cell at a current density of 5 mA cm^{-2}. Figures 2 A-C show images of individual pits produced through

94 focus variation microscopy, while Figures 2 D-F show the corresponding AFM images of the same surface locations. The

95 measurements conducted by the two microscopy techniques were consistent with regards to geometric shape and pit

96 dimensions.

97 To provide a quantitative comparison, the average width and maximum depth of each pit were measured. The

98 average pit width was calculated from the mean value of 180 cross-sectional measurements taken through the pit centroid.

99 Furthermore, the maximum pit depth was measured from the difference in depth between the surrounding bulk surface

100 and the lowest point in the pit. To differentiate the bulk electrode surface from the pit, a segmentation algorithm was

101 developed in MATLAB®. The algorithm applies a threshold to the luminance of the optical image in greyscale and to the

102   3D gradient of the spatial coordinates. Details of the algorithm, as well as analysis of the pit eccentricity and circularity,

103   are provided in the Supplementary Information.

104   Figures 2 G and H show the measured dimensions of each pit, demonstrating good agreement between the optical

105   microscope and AFM measurements. However, the time needed for data acquisition differs significantly between the two

106   microscopy techniques. The optical microscope performed each scan, spanning multiple pits, in approximately twenty

107   seconds, while the duration of an AFM scan for a single pit was approximately five minutes. This affords the optical

108   microscope superior temporal resolution for *operando* analysis, while simultaneously providing a larger field of view that

109   spans multiple pits. Therefore, focus variation microscopy is well suited to capture the dynamic morphology of the

110   working electrode surface throughout a dissolution half-cycle, as shown in Video 1 (Supplemental Information). In the

111   following discussion, this capability is used to quantify anisotropic pit expansion and demonstrate the role of

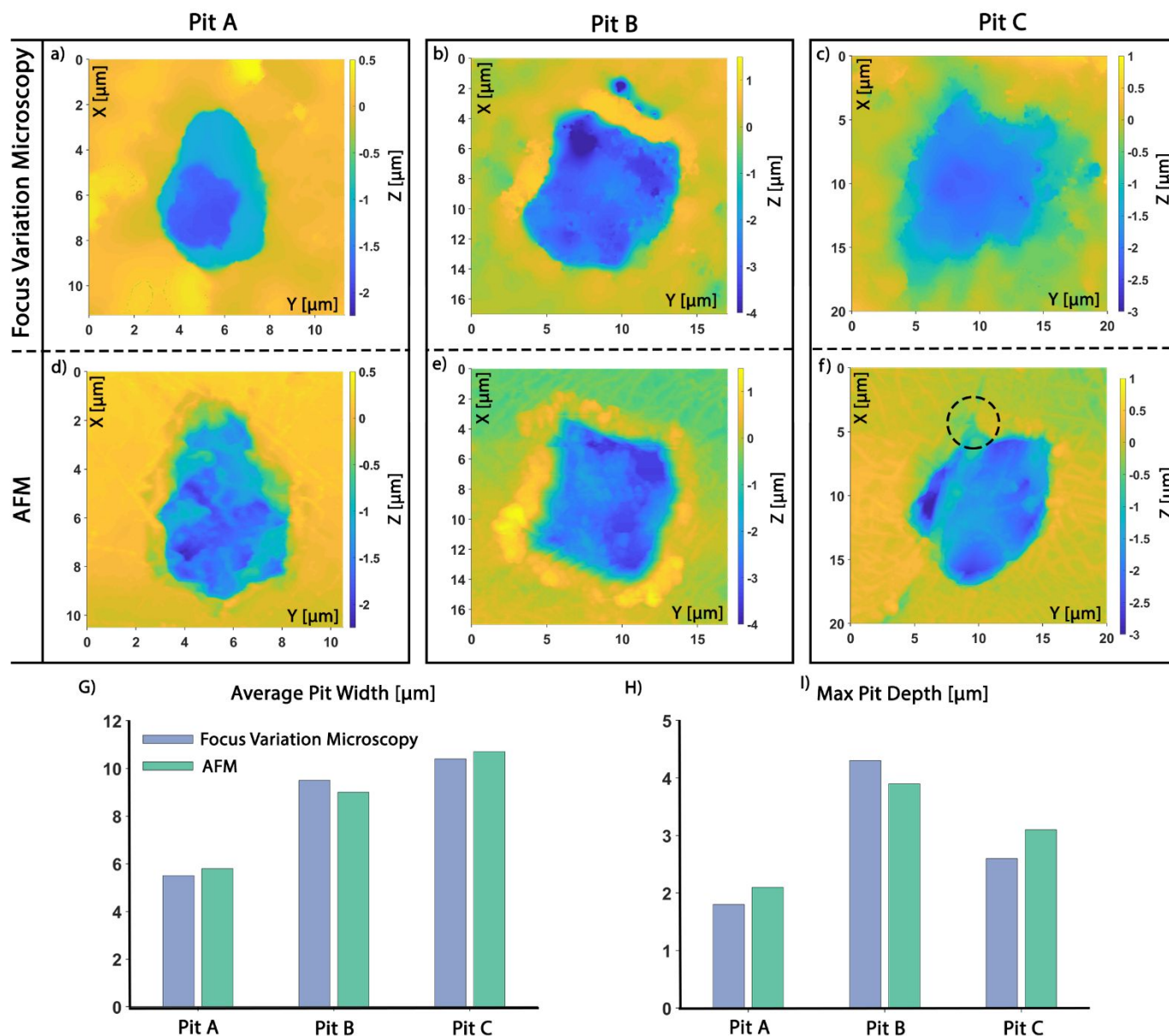112   crystallographic orientation and surface microstructure during electrodissolution.

Figure 2. Images of three different pits captured through a-c) *ex situ* focus variation microscopy and d-f) *ex situ* AFM on Li metal electrodes. Li was stripped at a current density of 5 mA cm^{-2} in each coin cell. The depth of discharge was 0.027 mAh cm^{-2} in Pit A (left column) ,0.041 mAh cm^{-2} in Pit B (middle column), and 0.055 mAh cm^{-2} in Pit C (right column). (g) The average pit width and h) maximum pit depth of for each pit were measured by focus variation microscopy and AFM.

Anisotropic In-Plane vs. Through-Plane Expansion of Individual Pits

To study the morphological evolution of individual pits, *operando* focus variation microscopy was performed on the working electrode of a Li-Li symmetric cell. An areal capacity of 1.1 mAh cm^{-2} was stripped at 5 mA cm^{-2} in a 1 M LiPF$_6$ in 1:1 v/v ethylene carbonate/ethyl methyl carbonate (EC:EMC) electrolyte. 3D reconstructions were generated at different points in the stripping half cycle, as shown in Figure 3 and Video 1. The centroid of the pit was calculated and plotted with a red sphere to quantitively track translational motion of the pit.

120   Figures 3 A-C present isometric views of the pit expansion where the centroid is observed to monotonically

121   translate in the negative Z-direction. This is expected since the pit expands into the bulk Li. However, there is negligible

122   translation of the centroid in the XY-plane. The centroid remains close to the coordinate origin and translates less than one

123   micron in the lateral directions. The lack of in-plane translation indicates that the expansion of the pit remains centered

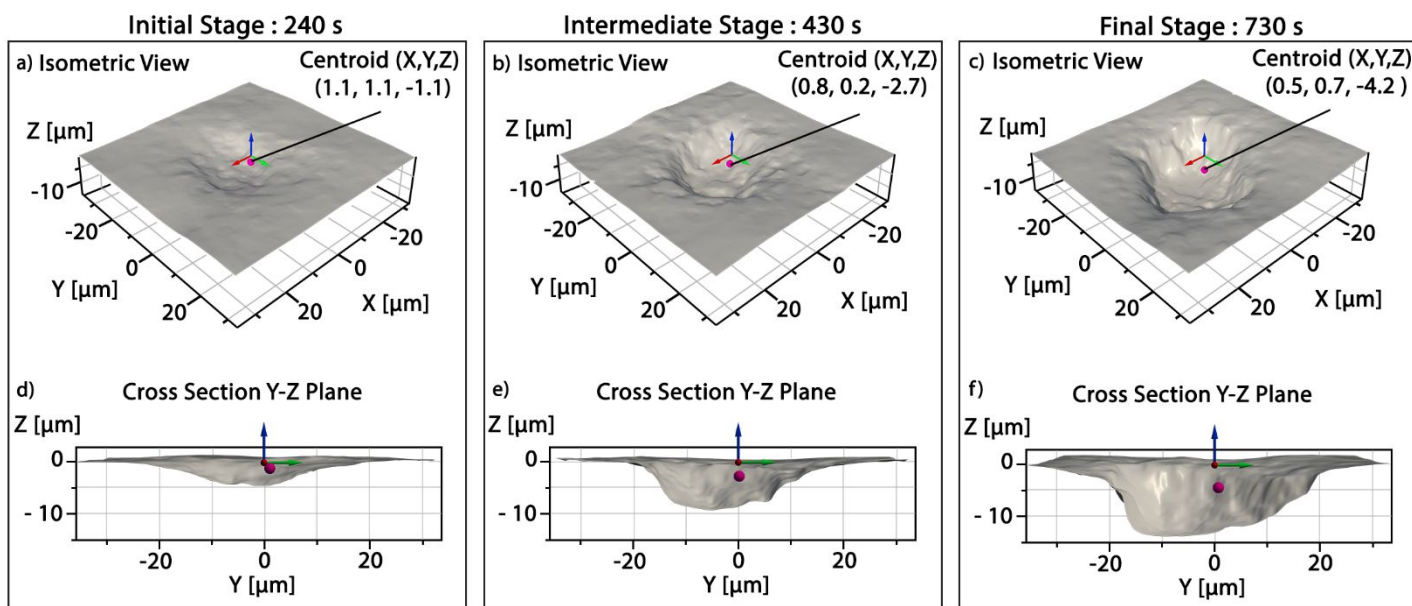124   around the initial nucleation point in the XY-plane.

125

Figure 3. 3D reconstructions of a pit from an a-c) isometric view and d-f) cross sections of pit along the YZ-plane produced by *operando* focus variation microscopy. Each column represents a point in time during the half cycle, 240 s (left column), 430 s (middle column), and 730 s (right column).

126   Strong anisotropy in the pit geometry was observed in the 3D reconstructions. Figures 3 D-F show cross-sections

127   of the pit along the YZ plane. In each frame, the pit width is consistently more than two times larger than the maximum

128   pit depth. Using the previously described segmentation method (Section 2) to define the pit edges, the pit width along the

129   YZ-plane expands from 38.2 μm to 58.3 μm, while the maximum pit depth increases from 4.9 μm to 13.6 μm. The

130   asymmetric profile of the pit cross-section demonstrates that the pit expands more rapidly in the in-plane directions than

131   in the out-of-plane direction.

132   To further quantify the anisotropy between the in-plane and out-of-plane directions, the aspect ratio of the average

133   pit width to the maximum pit depth was calculated throughout the half-cycle. If pit expansion occurred in an isotropic

134   manner, an aspect ratio of 2 would be observed. However, the measured values remained greater than 3, indicating that

135   the pit width expanded faster than the pit depth. This trend was consistently observed across all pits along the electrode

136   surface (the aspect ratio as a function of time for multiple pits are provided in the Supplementary Information).

137   The observed anisotropic expansion will be influenced by crystallographic texture of the underlying Li electrode.

138   For example, Density Functional Theory (DFT) modeling of Li metal anodes has shown that the thermodynamic

139   overpotential for plating and stripping varies in different crystallographic directions.[38] The overpotential for stripping was

140   predicted to be higher on the {100} family of planes than on the {110} family, which will influence the relative rates of

141   electrodissolution according to Butler-Volmer kinetics (further discussion in the Supplementary Information). These

142   variations can drive anisotropic pit expansion similar to the results in Figures 3 D-F. For the Li foil used in this study, a

143   strong [100] out-of-plane orientation has been measured by pole-figure diffraction analysis, which is a consequence of the

144   rolling process commonly used to manufacture commercial Li foils.[39,40] Owing to the preferential [100] alignment in the

145   normal direction, a slower rate of electrodissolution will occur normal to the Li surface because of the higher stripping

146   overpotential relative to kinetically-fast crystallographic directions in the orthogonal in-plane directions.

147   Since Li is a body-centered-cubic system, the {100} family of planes is also present along the in-plane directions.

148   This should cause anisotropic in-plane expansion, with preferential stripping along kinetically-faster crystallographic

149   directions. As a result, facets can form as pits expand laterally, which will be described below. The anisotropic dissolution

150   demonstrated here for Li is analogous to the preferential stripping that occurs on the (0001) basal plane of Mg in a 1M

151   ethyl magnesium bromide electrolyte.[41]

152   Another factor that can contribute to dissolution anisotropy is the growth of surface films, such as the SEI. For

153   example, previous studies have suggested that the dissolution behavior of Mg is dependent on the growth of surface

154   films.[41,42] In a 0.01 M NaCl solution, the (0001) plane was shown to be the most resistant to dissolution, while in a 0.01 M

155   NaCl/0.00001 M Dichromate solution, the (0001) plane was less resistant to dissolution than the prismatic planes.[41,43]

156   Additionally in pitting corrosion of metals, anisotropic pit expansion has been attributed to the growth of surface films,

157   which is influenced by the crystallographic orientation of the substrate and by the presence of impurities and alloying

158   elements.[41,42,44,45] In Li metal, variations in the SEI growth rate along the electrode surface have been linked with spatially-

159   varying kinetic rate constants along the surface.[46] Thus, the anisotropic evolution of Li pit morphology shown here

160   motivates additional investigations of how SEI growth kinetics depend on surface orientation of Li metal grains[47], to

161   elucidate the role of surface films on spatially varying kinetics during stripping.[48] We also note that the anisotropic pit

162   expansion has also been observed in less reactive metals where an SEI does not form, such as 316L stainless steel.[49]

163   In addition to the crystallographic factors described above, a third contributing factor to the observed anisotropy

164   in Li pits is the geometric curvature of the pit edge, which can induce local current focusing.[50] This is consistent with our

165   previous observation that nucleation of Li plating preferentially occurs along the perimeter of pits formed in the previous

166   half-cycle, which has been shown to influence CE.[30]

167   Overall, the dependence of stripping overpotential on crystallographic direction, SEI formation, presence of

168   impurities, and current focusing can all contribute to the through-plane anisotropy observed in the *operando*

169   measurements. We hope that the experimental observations in this study will motivate future modeling work to

170   understand the dynamic interplay between thermodynamics, kinetics, and mass transport during anisotropic pit evolution.

171   In the following results and discussion, we further demonstrate the critical roles of crystallographic texture and surface

172   microstructure on pit morphology.

173   **Faceting of Pits During Expansion**

174   In addition to through-plane anisotropy, in-plane anisotropy was also observed. As individual pits grow in size,

175   faceted edges were observed to form along their perimeter. Figures 4 A-C show the geometric evolution of an individual

176   pit. To quantify this faceting behavior, the perimeter of the pit was discretized into equidistant points, and the normal

177   vectors of the edge were calculated at each point (Figures 4 D-F). The angle of each normal vector was then measured

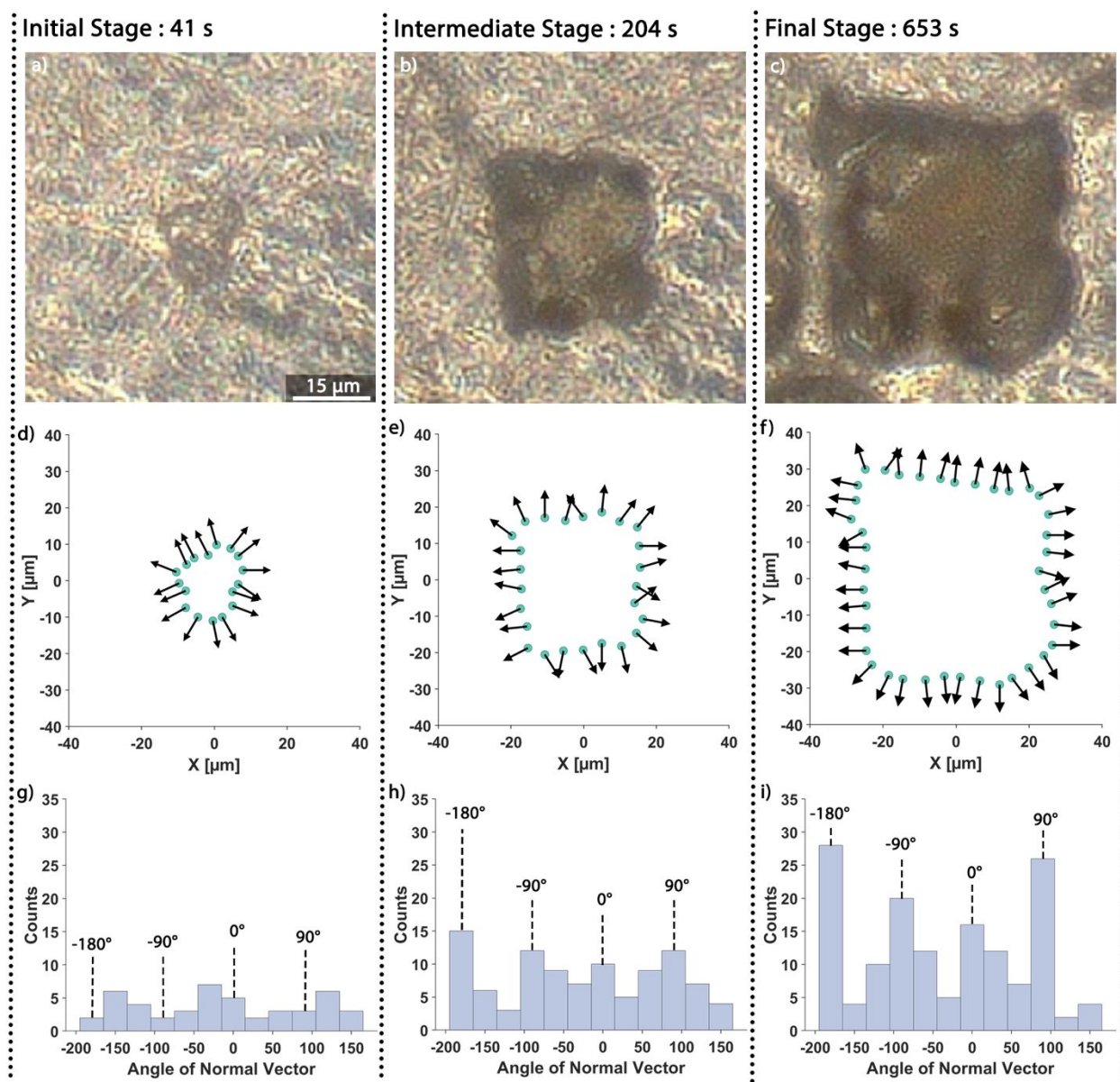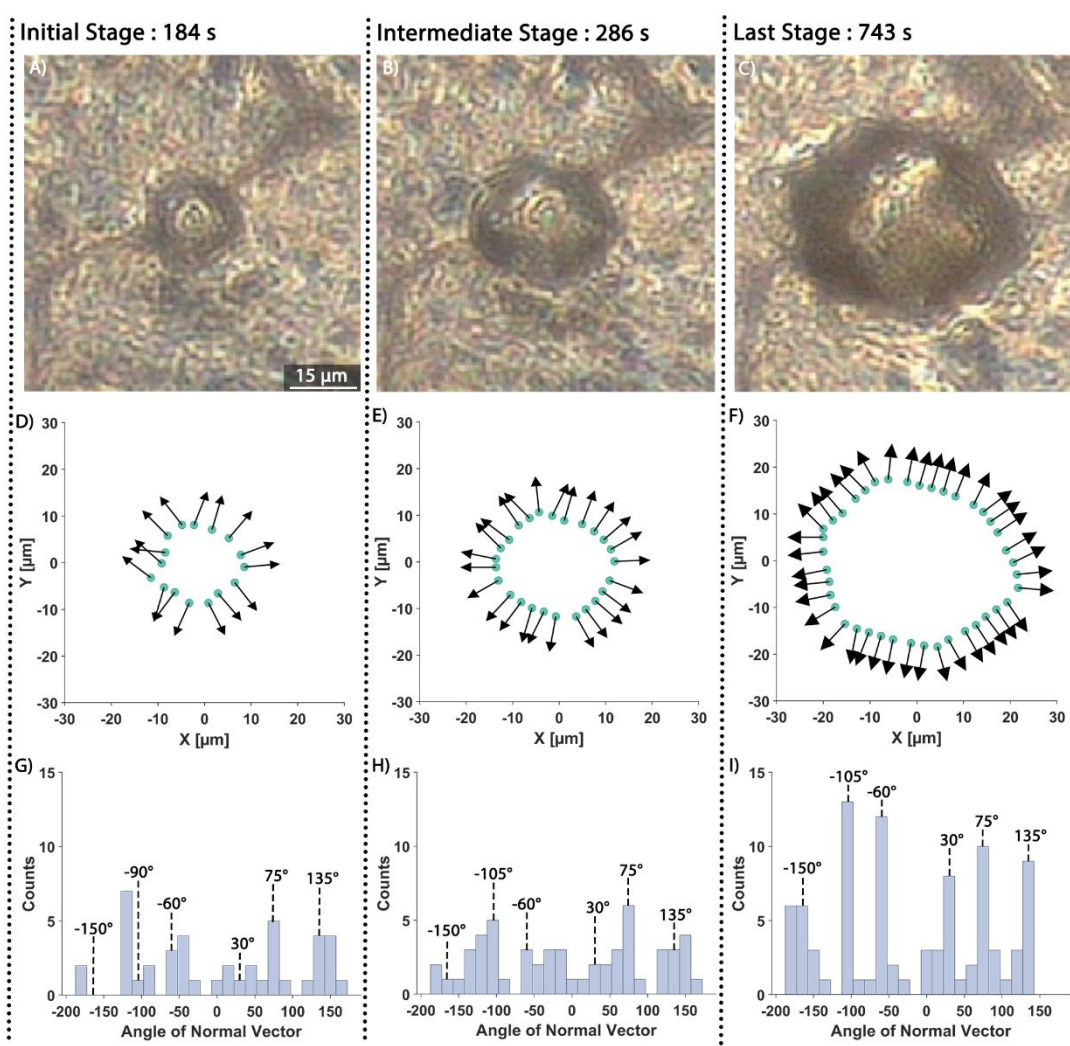178   with respect to the X-axis and binned into histograms as shown Figures 4 G-I.

Figure 4. a-c) Optical images of a pit, d-f) outlines of pit edge with normal vectors to pit edge, and g-i) histograms of all normal vector angles with respect to the X-axis at different points in time of the stripping half cycle, 41 s (left column), 204 s (middle column), and 653 s (right column).

179

180   In the initial stages of the half cycle, the pit morphology did not demonstrate any clear faceting (Figure 4 A). The

181   surface normal vectors pointed out radially (Figure 4 D), and the histogram (Figure 4 G) shows a relatively uniform

182   distribution. However, as the half-cycle progressed, the pit developed four-fold symmetry (Figure 4 B), as indicated by

183   grouping of the normal vector directions (Figure 4 E). The groups of angles are centered around -180°, -90°, 0° and 90°

184   (Figure 4 H). The grouping of normal vector angles indicates that facets developed at the pit edge. The four-fold

185   symmetry and facets observed in the middle column of Figure 4 were maintained as stripping proceeded, as shown in

186   right con of Figure 4.

187   The results above provide further evidence that crystallographic texture is a contributing factor in the anisotropic

188   dissolution of Li metal. Analogous faceting behavior has been observed in pitting corrosion, where body-centered-cubic

189   metals, such as iron, have been demonstrated to form polygonal pits.[51] These facets can develop when the dissolution rate

190   varies with respect to the crystallographic planes.[45,52] Moreover, the quadrilateral shape displayed in Figure 4 was not the

191   only polygonal shape observed. Other examples of faceting, such as pentagons and hexagons, were also commonly

192   observed. An example of a hexagonal pit is shown in Figure 5. The variations in shapes indicate that other factors, in

193   addition to the crystallographic texture, contribute to dissolution anisotropy. One important factor is the Li surface

194   microstructure, which is described below.

195

Figure 5. a-c) Optical images of a pit, d-f) outlines of pit edge with normal vectors to pit edge, and g-i) histograms of all normal vector angles with respect to the X-axis at different points in time of the stripping half cycle, 184 s (left column), 286 s (middle column), and 643 s (right column).

196

197

Influence of Electrode Microstructure on Pit Morphology

199   To explore the impact of the Li microstructure on dissolution anisotropy, pit expansion was studied near surface

200   grain boundaries. Figures 6 A-C show the growth of a pit throughout the stripping half-cycle. To quantify the influence of

201   the surrounding surface grain boundaries, the distance between the pit centroid and the edge was measured at varying

202   polar angles. These measurements are shown in Figures 6 D-F where the radial distance from the pit center to the edge is

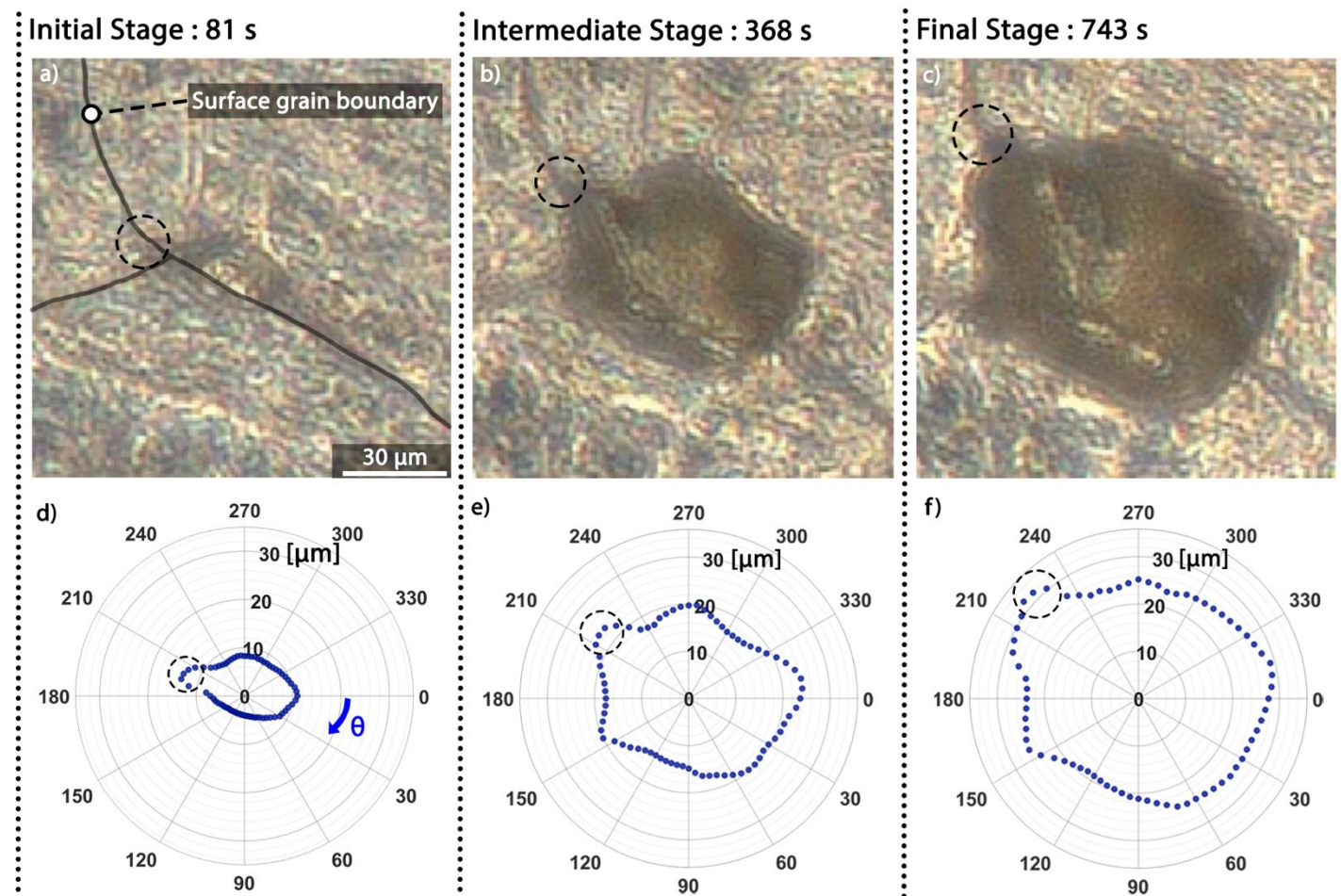203   expressed a function of polar angle (θ).

Figure 6. a-c) Optical images of a pit and d-f) polar plots showing the radial distance from the pit center to the edge as a function of polar angle θ at different points in time of the stripping half cycle, 240 s (left column), 430 s (middle column), and 730 s (right column).

205   Consistent with previous results, the pit shown in Figure 6 developed facets during the intermediate stages of the

206   stripping half-cycle. However, an additional source of in-plane anisotropy was observed. Throughout all stages of the

207   stripping half-cycle, preferential pit expansion was observed along a surface grain boundary. The intersection of the pit

208   with this surface grain boundary is labeled with a dashed circle. A local apex was observed in Figures 6 D-F at this

209   intersection, indicating more rapid expansion along the surface grain boundary.

210   We note that preferential expansion was not observed along all the surface grain boundaries labeled in Figure 6 A.

211   For example, no apex is present at $\theta = 30°$ in Figures 6 D-F. In our previous publication, preferential nucleation of pits

212   was observed along surface grain boundaries.[30] However, not all nucleation "hot spots" were along grain boundaries, and

213   not all grain boundaries were hot spots. The same trend is exhibited during the expansion of pits shown here. Not all

214   surface grain boundaries cause preferential pit expansion, which may be attributed to variations in local kinetics and/or

215   diffusion along grain boundaries with different angular mismatch between the adjacent grains. For example, recent

216   modelling work has shown that the self-diffusion of Li can play an important role in the morphological evolution of the

217   electrode-electrolyte interface[53], which will be influenced by surface grain boundary orientation. Overall, the results

218   highlight the importance of the Li microstructure on the morphological evolution of the electrode surface.

219   To further study the influence of the Li microstructure on dissolution anisotropy, pit morphology was tracked with

220   respect to the surrounding grains. Figures 7 A-C show optical images of two pits expanding from the experiment

221   described in Figure 3 and Video 1. These pits nucleated on the same surface grain boundary and were surrounded by the

222   same grains at the top and bottom of the images. The pits and surface grain boundaries are labeled in the corresponding
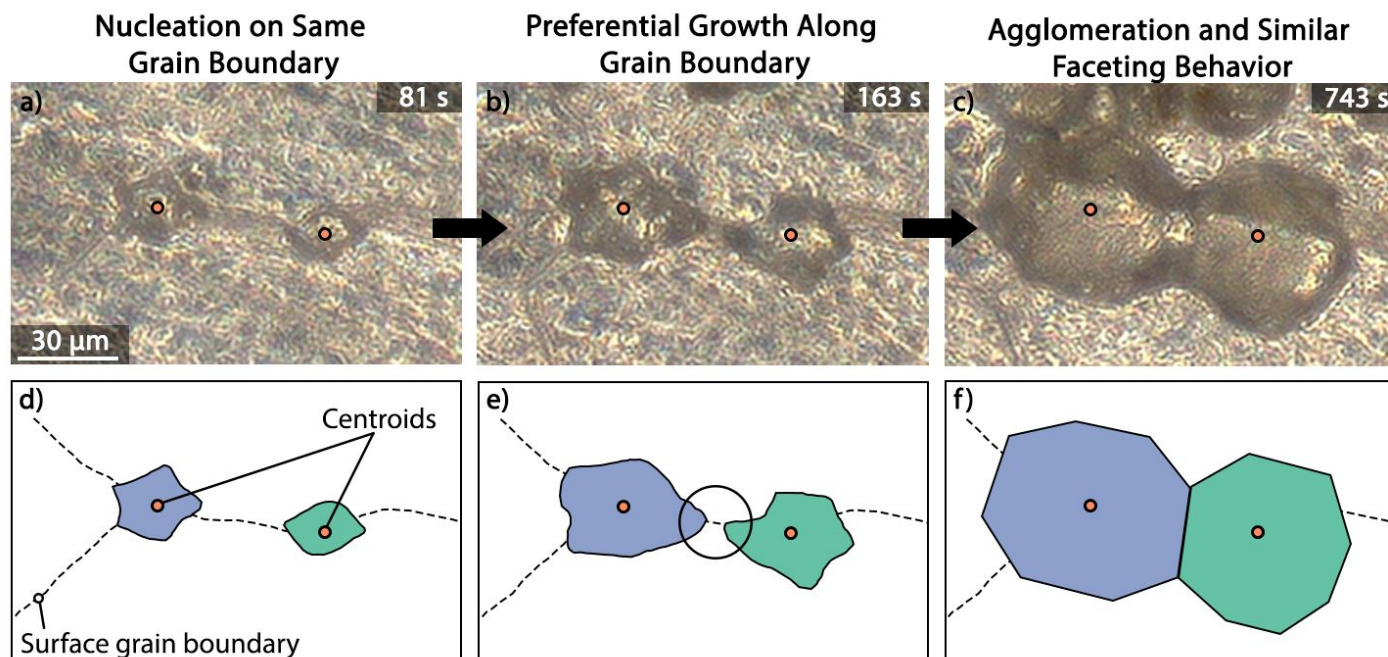
223   schematics in Figures 7 D-F.

224

Figure 7. a-c) Optical images of two pits with d-f) cartoon depictions at different points in time of the stripping half cycle, 81 s (left column), 163 s (middle column), and 743 s (right column).

225   Initially, the two pits nucleated on the same surface grain boundary and expanded into the same grains at the top

226   and bottom of the images as shown in Figure 7a,d. The preferential nucleation of pits along surface grain boundaries is

227   consistent with previous studies.[30] As these pits expanded, they preferentially grew along the surface grain boundary that

228   connects them (Figure 7b,e). Evidence for this is shown by the vertices along the pit edges that align with the surface

229   grain boundary. We also note that not all grain boundaries led to preferential pit expansion, as the right (green) pit

230   preferentially expanded along the boundary to the left, but not along the boundary to the right. Before merging, the

231   average width of these pits reaches 32.7 μm (left pit) and 27 μm (right pit), which is smaller than the average surface grain

232   size of the Li foil used in this study (150μm).[39] The merging of pits will be impacted by the grain size, since this

233   determines the distance between grain boundaries. At the end of the half cycle (Figure 7 right column), the pits formed

234   similar facets and display an octagonal shape with the same orientation.

235   In summary, multiple factors that lead to anisotropic in-plane expansion were demonstrated by the two pits shown

236   in Figure 7. Preferential expansion was observed along specific surface grain boundaries, and facets developed at

237   intermediate stages of the stripping half cycle. Additionally, the similar geometry (hexagons with parallel facets)

238   developed by the two pits suggest that the surrounding grains and grain boundaries impact the morphological evolution of

239   individual pits.

240   In contrast to its out-of-plane texture, the Li foil used in this study does not display a preferred in-plane

241   crystallographic texture based on pole-figure diffraction analysis.[39] Therefore, the directions of preferential in-plane pit

242   expansion will vary from grain to grain, and consequently the direction of pit facets are expected to also vary among

243   different grains. This helps to explain why different geometric shapes (rectangles, pentagons, hexagons etc.) can all be

244   observed in the same electrode. For example, the number of edges and interior angles of each polygon will be influenced

245   by both the underlying crystal structure and the angular misorientation between adjacent grains (further discussion in

246   Supplementary Information). However, in the case where multiple pits expand into the same set of grains (as shown in

247   Figure 7), the observed consistencies in polygonal shape and facet orientation can be rationalized by the underlying

248   crystal structure. Similar behavior is known to occur in pitting corrosion, where the pit polygonal shape can abruptly

249   change when crossing a grain boundary,[45] which is a direct result of the different orientation of the adjacent crystallite.

250   The parallel faceting among several adjacent pits was also observed in coin cells (Supplementary Information), which

251   confirms that the trends reported throughout this study also occur under cells with applied stack pressure and a polymer

252   separator. Overall, these results demonstrate that Li microstructure, grains and surface grain boundaries, all contribute to

253   the anisotropic expansion of pits on Li metal anodes.

254   **Implications of Anisotropic Pit expansion on Li Metal Anode Cycling**

255   The results of this study highlight the importance of the electrode crystallographic orientation and microstructure

256   on the morphological evolution of Li metal anodes during stripping (discharge). These properties of the electrode surface

257   directly impact pit morphology, which in turn plays a critical role in Li metal anode performance. For example, the pits

258   that form during stripping in the first cycle have been shown to improve the CE of the subsequent cycle.[30] This improved

259   reversibility is attributed to preferential nucleation of plated Li within pits, and the extent of this improvement was shown

260   to be sensitive to the size of the pits. Furthermore, the initial pits formed in the first cycle serve as the preferential

261   nucleation sites for subsequent plating throughout the extended cycle life of the electrode. It has also been shown that by

262   controlling the manner in which pits are formed in the first cycle, improved reversibility and cycle life can be achieved.[8,32]

263   Together, these observations suggest that by engineering the crystallographic texture and surface microstructure

264   of a Li metal anode, the evolution of pit morphology during stripping may be tuned to optimize CE and cycle life. An

265   image series of deposition within a faceted pit is shown in Figure 8 and Video 2 (Supplementary Information). Consistent

266   with previous studies, nucleation of plated Li preferentially occurred at the edges of the pit.[30] It has also been previously

267   shown that the reversibility (Coulombic efficiency) of plating and stripping is influenced by the local morphology at the

268   base of a mossy deposit, which is attributed to changes in the volume of remaining "dead Li".[30] The anisotropic pit

269   geometries observed in this study will therefore influence the base of the plated Li deposits in the subsequent cycle, which

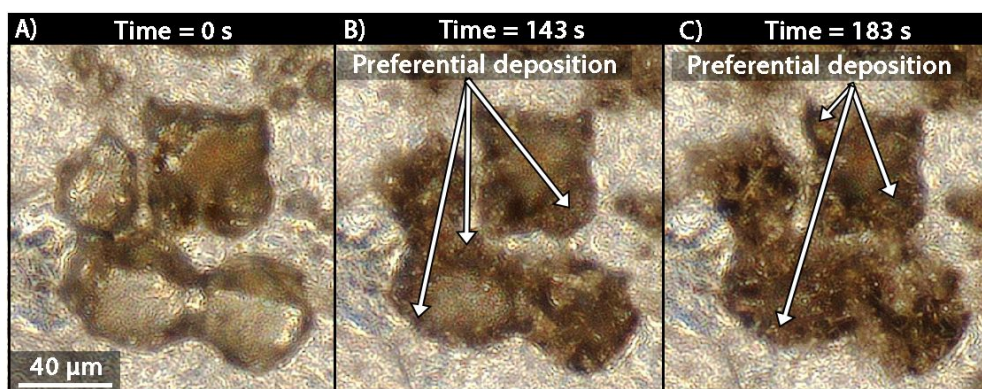270   could play a role in reversibility.

271

Figure 8. Optical images of deposition into faceted pits at a rate of 5 mA cm^{-2} at different points in time a) 0 s, b) 143 s, and c) 183s. Scale bar in a) the same for all images.

272   Metallurgical processing of the electrode could enable rational control of pit morphology. However, a practical

273   challenge facing the metallurgical processing of Li is the extreme reactivity of metallic Li. Therefore, future investigations

274   of process-structure relationships in manufacturing of Li metal batteries are needed to identify safe, scalable, and low-cost

275   methods to control the crystallographic and microstructural properties of Li metal. Moreover, it is important to note that

276   the electrode surface texture will continue to evolve when Li metal has been electrodeposited. Therefore, strategies are

277   needed to rationally control plated Li microstructure and grain orientation, including electrochemical conditions (e.g.

278   variations in current density and charging protocol),[54] as well as electrolyte composition.[40]

279   In addition to planar electrode geometries, the findings in this study also have implications for the design of 3-

280   dimensional electrode architectures, which have emerged as one of the most promising approaches to achieve high

281   reversibility in Li metal batteries.[6,7] For example, the size and morphology of plated Li can be influenced by steric

282   hinderances in porous 3-D electrodes, which can be further modified by control of surface chemistry and substrate-metal

283   interactions[6]. Further control of current collector geometry and surface chemistry in anode-free batteries could potentially

284   allow for control of crystallographic texture and grain orientation, including exploration of epitaxial relationships and

285   strain effects between the current collector and plated Li. This control, in turn, will influence stripping morphology, and

286   thus reversibility.

287   The anisotropic stripping of Li metal demonstrated in this study could also play an important role in dead Li

288   formation, which is a critical factor that influences CE and cycle life.[3,4] The transition from plated Li to dead Li is thought

289   to occur when Li is preferentially stripped from a region that results in electrical and/or electrochemical isolation from the

290   substrate.[3–5] Since Li metal dendrites have been shown to exhibit faceting and preferential growth directions,[55] these

291   microstructural characteristics will influence stripping along the deposited Li surface. As charge is removed from the

292   deposit, preferential stripping can occur as a consequence of the crystallographic texture and local geometry of the

293   deposited metal. These factors will be further influenced by preferential diffusion pathways along the plated Li surface[53],

294   including surface grain boundaries. This can drive a rapid decrease in the dendrite dimensions along the specific

295   crystallographic directions and microstructural features associated with anisotropic stripping, causing the isolation of a

296   dendrite or mossy Li deposit.

297

298   **<u>Conclusions</u>**

299   In conclusion, in this work, a platform for *operando* focus variation microscopy was introduced and used to map out

300   the morphological evolution of individual pits in 3-dimensions. Using this platform, the following insights were gained

301   into the dynamic behavior of the Li surface during stripping:

302   (1) Pits were observed to expand more rapidly along the surface of the Li electrode (in-plane) than into the depth of

303   the electrode (through-plane). The aspect ratio of several pits was consistently measured to be greater than 3.

304   (2) Pits were observed to develop faceted edges at intermediate stages of a stripping half cycle. The various polygonal

305   shape displayed by pits indicates that the underlying microstructure of Li plays an important role in the

306   morphological evolution of a pit.

307   (3) Pit morphology is impacted by surface microstructural features, including the orientation of grain boundaries and

308   the surrounding grains. Pit expansion was observed to preferentially occur along specific surface grain

309   boundaries. Furthermore, pits expanding into the same grains displayed similar morphologies, while pits

310   expanding into different grains displayed distinct morphologies.

311   Overall, the results of this study highlight the importance of the electrode crystallographic orientation and microstructure

312   on cycling. These two properties both influence anisotropic expansion of pits during stripping. The results point towards a

313   potential pathway to achieve improved performance through rational control of the electrode crystallographic orientation

314   and microstructure, both during manufacturing and subsequent plating. Additionally, the results suggest that dead Li

315   formation may be impacted by anisotropic stripping, which will be influenced by the crystallographic texture and surface

316   microstructure of individual Li deposits. In the future, further analysis of the influence of cycling conditions, electrolyte

317   composition, and external variables will be valuable to guide strategies to rationally control pit morphology.

318   **Experimental Section**

319   Details of the *operando* plan-view cell can be found in the SI. The electrolyte used in all experiments was 1M LiPF6 in

320   1:1 v/v EC/EMC (Soulbrain) and 750 μm thick Li foil (Alfa Aesar) was used as the electrodes. All cells were assembled

321   in an Argon glovebox with oxygen and water levels below 0.5 ppm. Coin cell electrodes were punched to an area of

322   1.76cm^2, while the plan-view electrodes were cut to size with a razor blade. AFM imaging was conducted on a MFP-3D

323   Origin+ (Asylum Research) in tapping mode. A Keyence VHX-7000 digital microscope was used for all optical

324   microscopy analysis. The 5000x objective was used for *ex situ* measurements while the 400x objective was used for

325   *operando* measurements. All image analysis was performed in MATLAB®.

326

Conflicts of Interest

328   The authors declare no competing interests.

Acknowledgements

337

References

339   1   W. Xu, J. Wang, F. Ding, X. Chen, E. Nasybulin, Y. Zhang and J. G. Zhang, *Energy Environ. Sci.*, 2014, **7**, 513–

340   537.

341   2   D. Aurbach, A. Zaban, Y. Gofer, Y. E. Ely, I. Weissman, O. Chusid and O. Abramson, *J. Power Sources*, 1995,

342   **54**, 76–84.

343   3   C. Fang, J. Li, M. Zhang, Y. Zhang, F. Yang, J. Z. Lee, M.-H. Lee, J. Alvarado, M. A. Schroeder, Y. Yang, B. Lu,

344   N. Williams, M. Ceja, L. Yang, M. Cai, J. Gu, K. Xu, X. Wang and Y. S. Meng, *Nature*, 2019, **572**, 511–515.

345   4   K.-H. Chen, K. N. Wood, E. Kazyak, W. S. LePage, A. L. Davis, A. J. Sanchez and N. P. Dasgupta, *J. Mater.*

346   *Chem. A*, 2017, **5**, 11671–11681.

347   5   A. Kushima, K. P. So, C. Su, P. Bai, N. Kuriyama, T. Maebashi, Y. Fujiwara, M. Z. Bazant and J. Li, *Nano*

348   *Energy*, 2017, **32**, 271–279.

349   6   K.-H. Chen, A. J. Sanchez, E. Kazyak, A. L. Davis and N. P. Dasgupta, *Adv. Energy Mater.*, 2019, **9**, 1802534.

350 7 Y. Liu, D. Lin, P. Y. Yuen, K. Liu, J. Xie, R. H. Dauskardt and Y. Cui, *Adv. Mater.*, 2017, **29**, 1–8.

351 8 M.-H. Ryou, Y. M. Lee, Y. Lee, M. Winter and P. Bieker, *Adv. Funct. Mater.*, 2015, **25**, 834–841.

352 9 J. Becking, A. Gröbmeyer, M. Kolek, U. Rodehorst, S. Schulze, M. Winter, P. Bieker and M. C. Stan, *Adv. Mater.*

353 *Interfaces*, 2017, **4**, 1700166.

354 10 A. C. Kozen, C.-F. Lin, A. J. Pearse, M. A. Schroeder, X. Han, L. Hu, S.-B. Lee, G. W. Rubloff and M. Noked,

355 *ACS Nano*, 2015, **9**, 5884–5892.

356 11 E. Kazyak, K. N. Wood and N. P. Dasgupta, *Chem. Mater.*, 2015, **27**, 6457–6462.

357 12 Y. Zhao, M. Amirmaleki, Q. Sun, C. Zhao, A. Codirenzi, L. V. Goncharova, C. Wang, K. Adair, X. Li, X. Yang,

358 F. Zhao, R. Li, T. Filleter, M. Cai and X. Sun, *Matter*, 2019, **1**, 1215–1231.

359 13 J. Qian, W. A. Henderson, W. Xu, P. Bhattacharya, M. Engelhard, O. Borodin and J.-G. Zhang, *Nat. Commun.*,

360 2015, **6**, 6362.

361 14 X. Cao, X. Ren, L. Zou, M. H. Engelhard, W. Huang, H. Wang, B. E. Matthews, H. Lee, C. Niu, B. W. Arey, Y.

362 Cui, C. Wang, J. Xiao, J. Liu, W. Xu and J.-G. Zhang, *Nat. Energy*, 2019, **4**, 796–805.

363 15 J. Zheng, M. S. Kim, Z. Tu, S. Choudhury, T. Tang and L. A. Archer, *Chem. Soc. Rev.*, 2020, **49**, 2701–2750.

364 16 S. Jiao, J. Zheng, Q. Li, X. Li, M. H. Engelhard, R. Cao, J. G. Zhang and W. Xu, *Joule*, 2018, **2**, 110–124.

365 17 D. Lu, Y. Shao, T. Lozano, W. D. Bennett, G. L. Graff, B. Polzin, J. Zhang, M. H. Engelhard, N. T. Saenz, W. A.

366 Henderson, P. Bhattacharya, J. Liu and J. Xiao, *Adv. Energy Mater.*, 2015, **5**, 1400993.

367 18 X. Yin, W. Tang, I. D. Jung, K. C. Phua, S. Adams, S. W. Lee and G. W. Zheng, *Nano Energy*, 2018, **50**, 659–664.

368 19 S.-H. Yu, X. Huang, J. D. Brock and H. D. Abruña, *J. Am. Chem. Soc.*, 2019, **141**, 8441–8449.

369 20 J. Steiger, D. Kramer and R. Mönig, *J. Power Sources*, 2014, **261**, 112–119.

370 21 J.-H. Cheng, A. A. Assegie, C.-J. Huang, M.-H. Lin, A. M. Tripathi, C.-C. Wang, M.-T. Tang, Y.-F. Song, W.-N.

371 Su and B. J. Hwang, *J. Phys. Chem. C*, 2017, **121**, 7761–7766.

372 22 E. Kazyak, R. Garcia-Mendez, W. S. LePage, A. Sharafi, A. L. Davis, A. J. Sanchez, K. H. Chen, C. Haslam, J.

373 Sakamoto and N. P. Dasgupta, *Matter*, 2020, **2**, 1025–1048.

374   23   K. J. Harry, D. T. Hallinan, D. Y. Parkinson, A. A. MacDowell and N. P. Balsara, *Nat. Mater.*, 2014, **13**, 69–73.

375   24   M. L. Meyerson, J. K. Sheavly, A. Dolocan, M. P. Griffin, A. H. Pandit, R. Rodriguez, R. M. Stephens, D. A.

376   Vanden Bout, A. Heller and C. B. Mullins, *J. Mater. Chem. A*, 2019, **7**, 14882–14894.

377   25   X. Wang, G. Pawar, Y. Li, X. Ren, M. Zhang, B. Lu, A. Banerjee, P. Liu, E. J. Dufek, J.-G. Zhang, J. Xiao, J. Liu,

378   Y. S. Meng and B. Liaw, *Nat. Mater.*, 2020, **19**, 1339–1345.

379   26   P. Biswal, S. Stalin, A. Kludze, S. Choudhury and L. A. Archer, *Nano Lett.*, 2019, **19**, 8191–8200.

380   27   P. Bai, J. Li, F. R. Brushett and M. Z. Bazant, *Energy Environ. Sci.*, 2016, **9**, 3221–3229.

381   28   L. Gireaud, S. Grugeon, S. Laruelle, B. Yrieix and J.-M. Tarascon, *Electrochem. commun.*, 2006, **8**, 1639–1649.

382   29   F. Shi, A. Pei, D. T. Boyle, J. Xie, X. Yu, X. Zhang and Y. Cui, *Proc. Natl. Acad. Sci.*, 2018, **115**, 8529–8534.

383   30   A. J. Sanchez, E. Kazyak, Y. Chen, K. H. Chen, E. R. Pattison and N. P. Dasgupta, *ACS Energy Lett.*, 2020, **5**,

384   994–1004.

385   31   Y. Sun, Y. Zhao, J. Wang, J. Liang, C. Wang, Q. Sun, X. Lin, K. R. Adair, J. Luo, D. Wang, R. Li, M. Cai, T. K.

386   Sham and X. Sun, *Adv. Mater.*, 2019, **31**, 1–9.

387   32   Y. Huang, R. Pan, D. Rehnlund, Z. Wang and L. Nyholm, *Adv. Energy Mater.*, 2021, **11**, 2003674.

388   33   A. Aleshin, S. Bravo, K. Redquest and K. N. Wood, *ACS Appl. Mater. Interfaces*, 2021, **13**, 2654–2661.

389   34   F. Helmli, in *Optical Measurement of Surface Topography*, ed. R. Leach, Springer Berlin Heidelberg, Berlin,

390   Heidelberg, 2011, pp. 131–166.

391   35   M. Shang, T. Kuang, H. Zhou and F. Yu, in *Proceedings - 2020 12th International Conference on Intelligent

392   Human-Machine Systems and Cybernetics, IHMSC 2020*, 2020, vol. 2, pp. 17–21.

393   36   S. M. Bello, I. De Groote and G. Delbarre, *J. Archaeol. Sci.*, 2013, **40**, 2464–2476.

394   37   L. Newton, N. Senin, C. Gomez, R. Danzl, F. Helmli, L. Blunt and R. Leach, *Addit. Manuf.*, 2019, **25**, 365–389.

395   38   K. S. Nagy, S. Kazemiabnavi, K. Thornton and D. J. Siegel, *ACS Appl. Mater. Interfaces*, 2019, **11**, 7954–7964.

396   39   W. S. LePage, Y. Chen, E. Kazyak, K.-H. Chen, A. J. Sanchez, A. Poli, E. M. Arruda, M. D. Thouless and N. P.

397   Dasgupta, *J. Electrochem. Soc.*, 2019, **166**, A89–A97.

398   40   F. Shi, A. Pei, A. Vailionis, J. Xie, B. Liu, J. Zhao, Y. Gong and Y. Cui, *Proc. Natl. Acad. Sci. U. S. A.*, 2017, **114**,

399   12138–12143.

400   41   D. J. Wetzel, M. A. Malone, R. T. Haasch, Y. Meng, H. Vieker, N. T. Hahn, A. Gölzhäuser, J. M. Zuo, K. R.

401   Zavadil, A. A. Gewirth and R. G. Nuzzo, *ACS Appl. Mater. Interfaces*, 2015, **7**, 18406–18414.

402   42   G. L. Song and Z. Xu, *Corros. Sci.*, 2012, **54**, 97–105.

403   43   C. R. McCall, M. A. Hill and R. S. Lillard, *Corros. Eng. Sci. Technol.*, 2005, **40**, 337–343.

404   44   M. Yasuda, F. Weinberg and D. Tromans, *J. Electrochem. Soc.*, 1990, **137**, 3716–3723.

405   45   H. H. Strehblow and P. Marcus, *Corros. Mech. Theory Pract. Third Ed.*, 2011, 349–394.

406   46   K. N. Wood, E. Kazyak, A. F. Chadwick, K.-H. Chen, J.-G. Zhang, K. Thornton and N. P. Dasgupta, *ACS Cent.*

407   *Sci.*, 2016, **2**, 790–801.

408   47   S.-K. Otto, Y. Moryson, T. Krauskopf, K. Peppler, J. Sann, J. Janek and A. Henss, *Chem. Mater.*, 2021, **33**, 859–

409   867.

410   48   J. Rohrer and P. Kaghazchi, *ChemPhysChem*, 2014, **15**, 3950–3954.

411   49   C. Fong and D. Tromans, *Metall. Trans. A*, 1988, **19**, 2765–2773.

412   50   A. Jana, D. R. Ely and R. E. García, *J. Power Sources*, 2015, **275**, 912–921.

413   51   V. K. J. Vetter and H. H. Strehblow, *Berichte der Bunsen-Gesellschaft*, 1970, 1024–1035.

414   52   K. S. Shin, M. Z. Bian and N. D. Nam, *Jom*, 2012, **64**, 664–670.

415   53   D. Tewari, S. P. Rangarajan, P. B. Balbuena, Y. Barsukov and P. P. Mukherjee, *J. Phys. Chem. C*, 2020, **124**,

416   6502–6511.

417   54   K. N. Wood, M. Noked and N. P. Dasgupta, *ACS Energy Lett.*, 2017, **2**, 664–672.

418   55   Y. Li, Y. Li, A. Pei, K. Yan, Y. Sun, C. L. Wu, L. M. Joubert, R. Chin, A. L. Koh, Y. Yu, J. Perrino, B. Butz, S.

419   Chu and Y. Cui, *Science (80-.).*, 2017, **358**, 506–510.

420

421